SAM sees the light

Andrei Tokovinin, Roberto Tighe, Patricio Schurter, Rolando Cantarutti, Nicole van der Bliek, Manuel Martinez, Eduardo Mondaca, Andrés Montané, Wolnays Naudy Cortés

Cerro Tololo Inter-American Observatory, Casilla 603, La Serena, Chile

ABSTRACT

We present a progress report on the SOAR Adaptive Module, SAM, including some results of tests of the Natural Guide Star mode: image correction in the visible, performance estimates, and experiments with lucky imaging. We have tested methods to measure the seeing and the AO time constant from the loop data and compared the results to those of the stand-alone site monitor. Measurements of the instrument throughput and telescope vibrations are given. We report progress on the Laser Guide Star system implementation, including tests of the UV laser, test of the beam transfer optics with polarization control. We present the designs of the laser launch telescope and laser wavefront sensor.

Keywords: Laser Guide Star, Adaptive Optics

1. INTRODUCTION

SOAR Adaptive Module, SAM, will be a facility-class adaptive optics system for the 4.1-m SOAR telescope.[6,7,10] It will use the light of a Rayleigh laser guide star (LGS) to sense and compensate turbulence in low atmospheric layers. This is a variant of a ground-layer adaptive optics (GLAO) where the resolution is improved over natural seeing in a relatively wide field, but is still far from the diffraction limit. SAM will be able to improve seeing by as much as two times over a 3 arcmin field at visible wavelengths.

The design of SAM has been described in Refs. 7, 10. A pair of off-axis parabolic mirrors re-images the focal plane onto science instruments with 1:1 scale while correcting turbulence with a 60-element bimorph deformable mirror (DM). The wavefront sensor (WFS) is of Shack-Hartmann type, with 10x10 sub-apertures and an e2v CCD-39 detector. We set the AO loop time at 4.3 ms per cycle. In the LGS mode, tip-tilt will be sensed with two natural guide stars (NGS) located outside the main field.

As a first step, we tested the SAM in the NGS mode in 2009. The on-sky results are reported here briefly. We then focus on the design and tests of the remaining LGS sub-systems - UV laser, beam transfer, laser launch telescope, and LGS wave-front sensor.

2. SAM FIRST-LIGHT TESTS

SAM was installed at the telescope on August 5, 2009. During this engineering run, the weather was bad and we just managed to close the loop on a bright star seen through the clouds. During the next run, August 31 to September 3, the seeing was bad and fast. Some time was lost to clouds, so we observed a total of 1.5 nights. The third run consisted of the partially clear night of October 2 with normal to good seeing conditions. The instrument was removed from the telescope on October 4, 2009.

A neutral dichroic installed in SAM directed some 86% of the light to the WFS, the rest went to the High-Resolution Camera (HRCam). HRCam consists of an electron-multiplication CCD Luca from Andor placed after 1:2 magnifying optics.[12] The pixel scale is 15.3 mas, the field of view is 7.5x10 arcseconds. Series of 400 images with 20 ms exposure time were recorded for further processing. In parallel, we frequently saved the loop data (WFS slopes and DM voltages) for further off-line analysis.

E-mail: atokovinin, rtighe, pschurter, rcantarutti, nvdbliek, mmartinez, emondaca, amontane, wnaudy@ctio.noao.edu

Figure 1. SAM is being lifted from the dome floor to the Nasmyth platform of SOAR on August 5, 2009.

2.1 Compensated image quality

Compensated images of single and binary stars were analyzed to determine the resolution gain. In the case of binaries, we measured the relative position and brightness of the pair by means of speckle-interferometry processing of the data cube[12] and then de-convolved the image to obtain the point-spread function (PSF). The PSFs were azimuthally averaged.

Averaging all instantaneous images in the data cube simulates a long exposure (typically up to 12 s). When the star is sufficiently bright to give several photons per speckle, angular resolution can be gained by selecting the best images and co-adding them after re-centering on the brightest pixel. This method is known as "shift-and-add" or as "lucky imaging".[1] We found that selecting best images by the maximum intensity (brightest speckle) gives better results compared to selecting by sharpness or by second moment. The "lucky" processing was applied to all data cubes with a selection threshold of 20% (i.e. co-add 80 best images out of a cube with 400 frames).

Figure 2 shows example of a binary star with a faint companion, comparing simple average with lucky imaging. On the right-hand plot such comparison is done for a representative number of other PSFs spanning a range of seeing conditions (observations on October 2). The seeing was estimated from the AO loop data es explained below. Typically, the FWHM with lucky imaging is 2/3 of the long-exposure FWHM. Under good seeing the additional gain brought by lucky imaging becomes less. The average FWHM for the data sub-set plotted in Fig. 2 is $0.21''$ for long exposure and $0.15''$ for lucky imaging.

The radial profiles of the compensated PSFs are plotted in Fig. 3 for two representative cases. As expected, the AO-compensated PSF has a narrow core and wings, with a radial profile resembling a negative exponent, rather than Gaussian. The Gaussian profiles with FWHM corresponding to the seeing are plotted for comparison. We calculated the residual structure function (SF) of the optical path difference $D_l(\mathbf{r})$ by Fourier transform of the long-exposure PSFs $\tilde{P}(\mathbf{f})$, taking advantage of the relation

$$\tilde{P}(\mathbf{f}) = \exp[-0.5(2\pi/\lambda)^2\ D_l(\lambda\mathbf{f})], \tag{1}$$

where $\mathbf{f}$ is the angular frequency in rad^{-1} and λ is the imaging wavelength. The initial segment of the SF is close to linear, with a slope depending on the seeing. This slope ranges from 0.15 to 0.3 $\mu\mathrm{m}^2/\mathrm{m}$. This is close to the expected performance of SAM.[9]

2.2 Estimation of atmospheric parameters from the AO loop data

During the testing of SAM, the atmospheric parameters were measured by the Cerro Pachón MASS-DIMM site monitor installed in a small tower.[8] It observed bright stars.

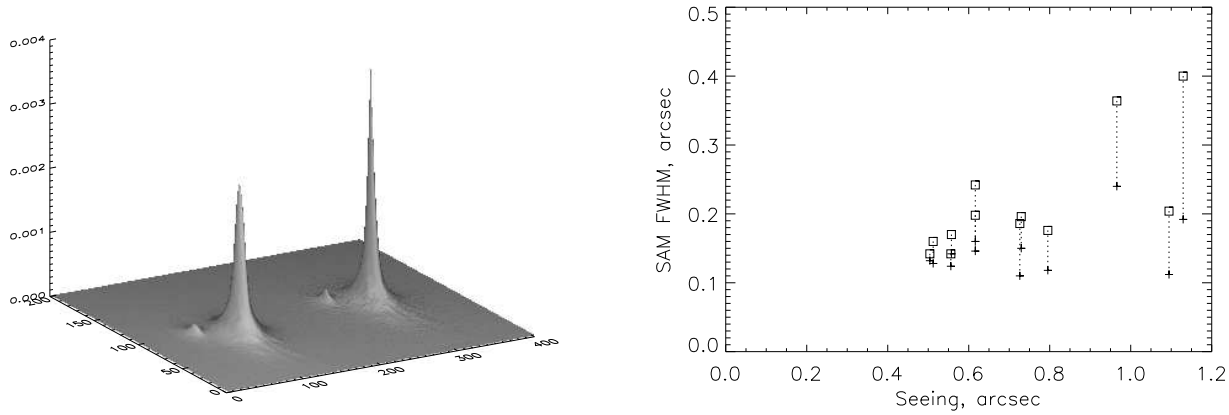

Figure 2. **Left:** Surface plot of the two images of binary star Msn 1 (separation $0.70''$, $\Delta m = 3.3$) in the I-band. The left image corresponds to simple averaging of the data cube, the right image – to selection of the best 20% instantaneous images and re-centering (lucky imaging). **Right:** Relation between the atmospheric seeing (horizontal axis) and the FWHM of the compensated images in the case of averaging (squares) and "lucky" processing (crosses connected to squares) for a sub-set of data of October 2, 2009.

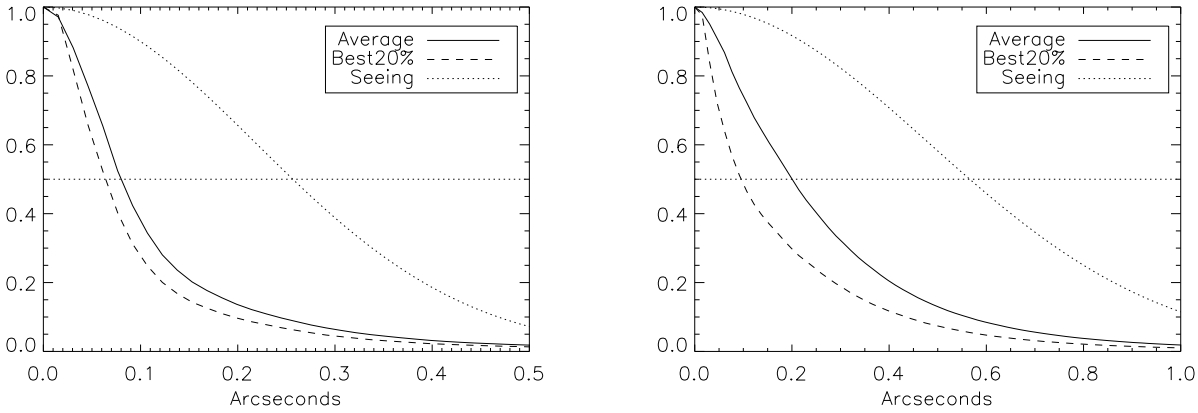

Figure 3. Radial profiles of the PSF normalized to maximum under good (left) and mediocre (right) seeing conditions. Full lines correspond to long-exposure corrected PSFs, dashed lines – to lucky processing, dash-dotted – to seeing.

The SAM loop data were processed using an IDL program to estimate atmospheric parameters. Zernike coefficients of atmospheric wave-fronts were calculated from the DM voltages and WFS slopes. The voltages were first converted into slopes using the measured interaction matrix. Subsequently the slopes were translated into Zernike coefficients with the help of the theoretically calculated gradient matrix G (we multiplied the slopes by the pseudo-inverse of G). A calibration coefficient was applied to convert measured slopes from pixels into radians at standard wavelength $\lambda = 500\,\mathrm{nm}$. Open-loop Zernike coefficients were reconstructed as a sum of DM and WFS coefficients, taking into account their relative delay of two loop cycles.[2]

The variances of the coefficients are calculated. The ratio of measured variances to the Noll coefficients[4] should equal $(D/r_0)^{5/3}$ for a Kolmogorov turbulence. In practice, we average this ratio for modes from 7 to 19 and calculate r_0 from this average. As shown in Fig. 4, the estimates of atmospheric seeing $\varepsilon_0 = 0.98\lambda/r_0$ delivered by SAM are in reasonable agreement with the DIMM, considering that we do not correct the SAM seeing to zenith and that the two instruments measure the seeing on different paths.

Temporal evolution of atmospheric wave-front distortions is characterized by the atmospheric coherence time $\tau_0 = 0.31 r_0/\overline{V}$, where $\overline{V}$ is the turbulence-weighted wind speed. This parameter can be calculated from the profiles of turbulence and wind speed measured, e.g., by a SCIDAR. Alternatively, an approximate estimate

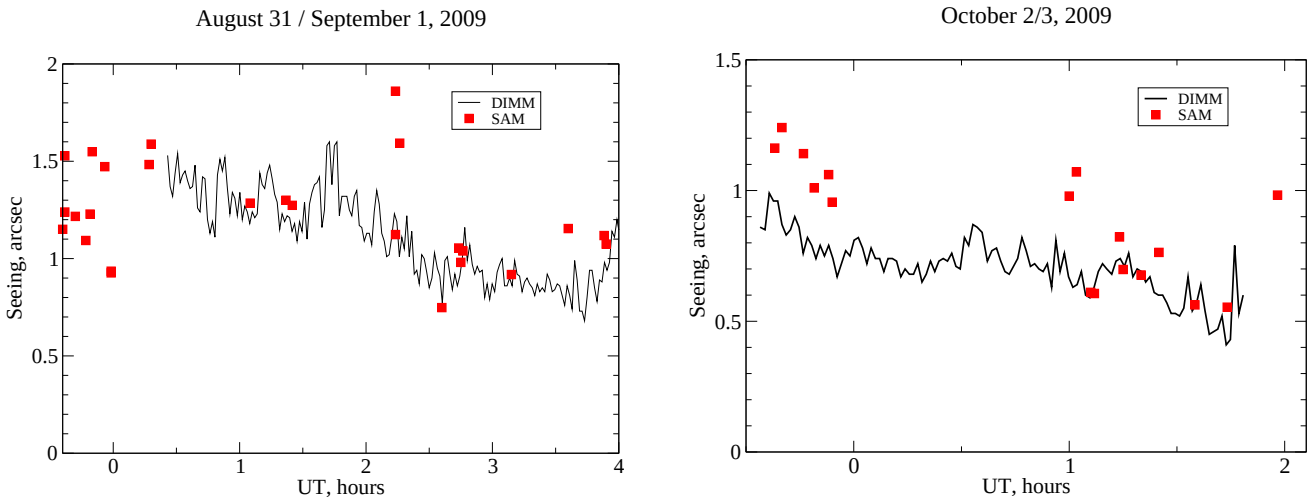

Figure 4. Atmospheric seeing as measured by the DIMM (full line) and estimated from the SAM loop data (squares) for the nights of August 31 (left) and October 2, 2009 (right).

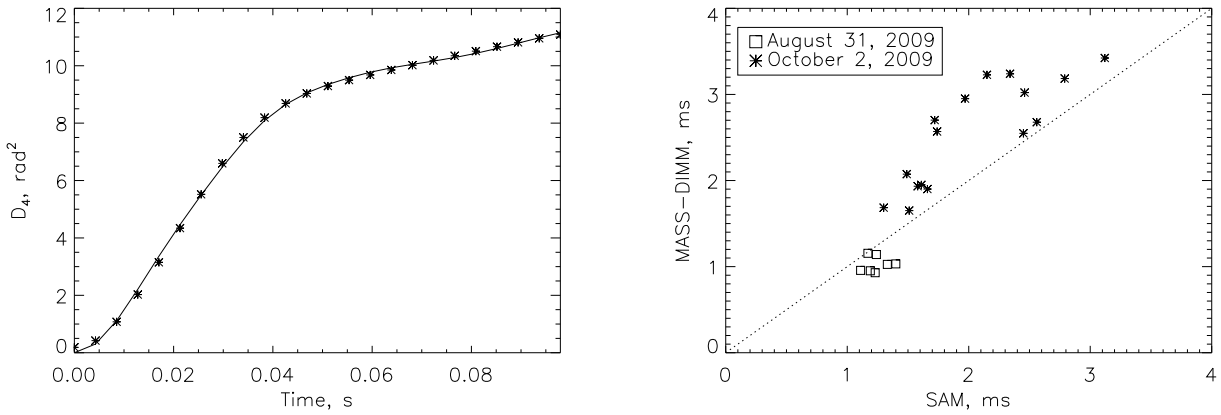

Figure 5. Estimation of the atmospheric time constant from defocus variation. **Left:** Measured temporal structure function of defocus Zernike coefficient (asterisks) and fitted model (line). **Right:** comparison of the τ_0 estimates by SAM and by MASS.

of τ_0 can be obtained from stellar scintillation with MASS.[13] Recently, it has been shown that the speed of atmospheric defocus variation provides a very good measure of τ_0. This FAst DEfocus (FADE) technique[11] can be easily applied to the AO loop data. We calculate the temporal SF of the atmospheric Zernike focus coefficient a_4 as follows. The power spectrum of a_4 on the DM is truncated at $\nu > 45\,\mathrm{Hz}$ to remove noise and vibrations, multiplied by the inverse square modulus of the AO loop frequency transfer function and Fourier-transformed to obtain the covariance and SF. The SF is fitted by a two-layer model, as explained in Ref. 11. The values of τ_0 derived in this manner depend on the length of the fitted SF part (smaller τ_0 if less points are fitted). Figure 5 shows an example of such fit and the comparison of τ_0 measurements by this method with simultaneous data from the MASS site monitor. On August 31, the wind speed at 200 mB level (in the tropo-pause) was up to 70 m/s, while on October 2 the wind speed was about 30 m/s. Both instruments clearly show the difference between these two nights.

Another method of estimating τ_0 from AO loop data was proposed by Fusco et al.[2] and implemented in the NAOS system at the VLT. It is based on the measured width of temporal covariance functions of Zernike coefficients, interpreted in the framework of a single turbulent layer. The authors claim that in the case of

multi-layer turbulence their method gives some average τ_0. In fact it rather measures the speed of the strongest layer. Considering that τ_0 depends on the wind speed as $V^{5/3}$, this parameter is mostly influenced by the fastest (rather than strongest) layers. We believe that the FADE technique should give less biased results because it ensures the correct V-weighting of multi-layer turbulence. The SAM real-time software provides estimates of r_0 and τ_0 "on the fly".

2.3 Other results

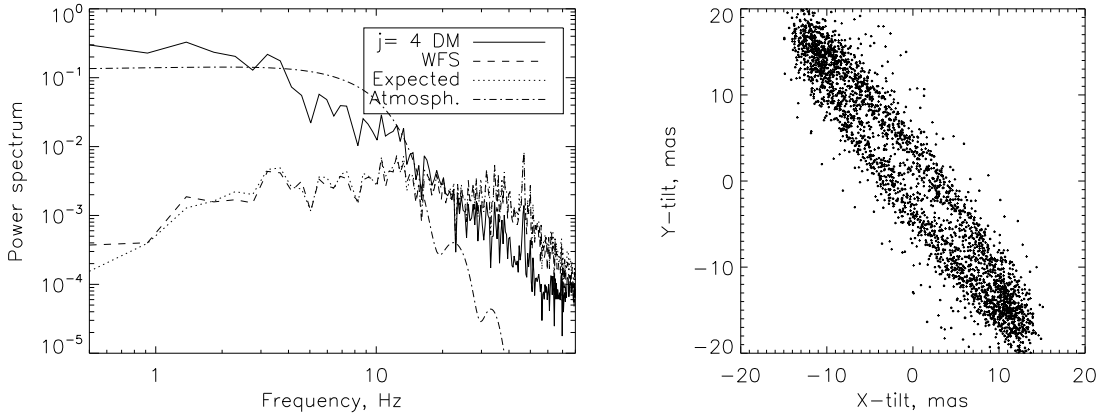

Figure 6. Vibrations recorded with SAM. **Left:** Temporal spectra of the Zernike defocus coefficient a_4 reconstructed from the loop data of August 31. Full line – input disturbance, dashed line – residual on the WFS, dotted line – input multiplied by the servo transfer function, dash-dotted line – theoretical spectrum for a single turbulent layer with a wind speed of 40 m/s. **Right:** Angular vibration at 50 Hz reconstructed from the tip and tilt coefficients recorded on October 2. The amplitude and shape of the ellipse change during the night.

Temporal spectra of Zernike coefficients show the expected behavior of the AO loop: correction of low temporal frequencies and slight amplification of high frequencies above the 0-dB crossover frequency. The amount of this over-shoot depends on the control parameters. Considering the relatively slow SAM loop with a 2-cycle delay, we used mostly the Smith predictor controller which gives a stronger over-shoot but smaller residuals compared to the standard integrator.[3] Figure 6, left, gives an example of such power spectrum for the defocus coefficient. Note that the power at high frequencies decreases approximately as $\nu^{-2.5}$, much slower than the theoretical slope of $-17/3$.[5] This behavior is observed always, even in the simulated data; it is likely caused by the imperfect reconstruction of the a_4 coefficient from slopes and the slope errors of atmospheric origin.

Apart from the slow decay at high frequencies and servo over-shoot, we see some narrow "lines" presumably caused by vibrations. Such lines are noted only on low-order coefficients (up to the astigmatism a_6). The defocus typically has a line at 45 to 47 Hz (as shown in Fig. 6), the astigmatisms have additional power between 60 and 65 Hz, the tip and tilt almost always have a line at 50 Hz. We studied the 50-Hz vibration by isolating this signal in the Fourier space, filtering out the servo response, and plotting the a_3 against a_2, both expressed as angular shifts. This procedure reveals that the 50-Hz vibrations on both axes are coherent, so that the line of sight describes an ellipse. The amplitude, orientation, and eccentricity of this ellipse change from one pointing to the other. In the worst cases, the rms amplitude reaches 20 mas, but it can be as low as 3 mas. The 50-Hz vibration was noted previously by M. Warner in the signal of the SOAR guiders; he found that it originates in the servo control of the SOAR tip-tilt mirror M3. Work is in progress to change the M3 electronics. The origin of vibrations in focus and astigmatism remains unclear, it could be an instrumental artifact rather than real fast distortion at the telescope. No such vibrations are seen when SAM closes the loop on its internal light source.

We determine the throughput of the SAM WFS channel from the data of the August 31 clear night. The flux F in the WFS (electrons per sub-aperture per loop cycle) is related to the stellar magnitude V of the guide star as

$$2.5 \log_{10} F + V \approx 16.40 + 0.44(B - V), \tag{2}$$

where the color term $0.44(B - V)$ accounts for the red sensitivity of the WFS. This equation tells us that a star of $V = 11.4^m$ will give a flux of 100 electrons per sub-aperture, still sufficient to run the loop. The overall quantum efficiency of the SAM WFS can be estimated at 30%, with a large uncertainty due to the undefined spectral response of the WFS.

3. PROGRESS TOWARDS SAM LGS MODE

3.1 Tests of the UV laser

The laser guide star for SAM will be created by a pulsed frequency-tripled Nd:YAG laser projected on the sky through a small telescope. We received the laser Q301-HD from JDSU in December 2008. A series of tests was performed to ensure that the laser works to specifications, but also to train ourselves. Indeed, we initially committed several errors. For example, the UV beam was attenuated by a "sampler" mirror with 99% reflectivity at 355 nm, transmitting 1% with $\lambda/10$ quality. However, this mirror is transparent at longer wavelengths. We also found that a standard neutral-density filter of optical density of 1 in the visible has a density 2.4 at 355 nm. As a result, we were unwittingly measuring the residual light from the 1-st and 2-nd harmonics instead of the UV. The correct way is to always use the UG-11 Schott UV filter in front of the detector.

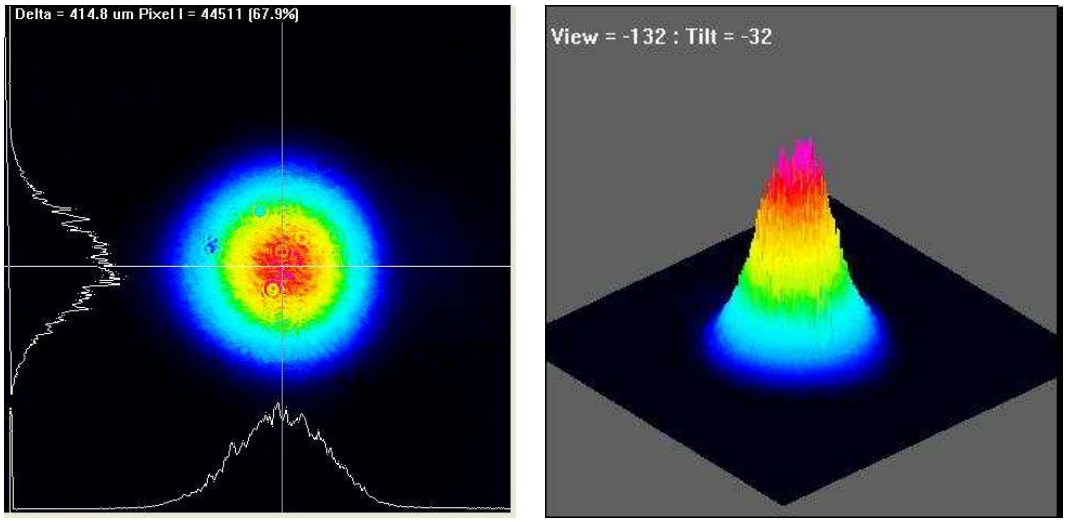

Figure 7. Gaussian profile of the UV beam at full power, 10 W.

The beam profile was measured with the Beamage CCD23 detector from Gentec. The beam is found to be nearly Gaussian with the expected $1/e^2$ diameter $2W$ of 1.67 mm at 0.5 m distance from the laser (Fig. 7). The power reaches its nominal value of 10 W at pulse repetition frequency of 10 kHz. At low power, the beam becomes slightly elliptical (narrower in the horizontal direction and wider in the vertical direction).

The beam quality was determined by scanning through the focus, measuring W, and fitting the $W(z)$ curve to the formula $W^2 \approx W_0^2[1 + (\theta z)^2]$ with two parameters (W_0, θ). The resulting beam quality $M^2 = \pi(\theta W_0)/\lambda$ is 1.05 in both horizontal and vertical directions (the specification is $M^2 < 1.2$). Therefore, the UV beam is essentially a perfect single TEM00 mode. The laser pulse length was measured to be 36 ns, in agreement with the specifications.

Linearly polarized laser light will be transformed into circular polarization when launched into the sky. This way, we expect to receive circularly-polarized return signal from the Rayleigh scatter, allowing for the relative rotation between SAM and telescope without light loss (the Pockels-cell shutter in the WFS works in polarized light). We studied the polarization components required for these transformations and measured the phase shifts introduced by oblique reflections from dielectrically coated laser mirrors. As a result, we found that a suitably

oriented $\lambda/4$ plate in the laser launch telescope (LLT) will be sufficient for getting a circularly plarized beam. Another such plate will be installed in the WFS, converting the circular polarization back to linear. Of course, only 1/2 of the un-polarized component of the return signal produced by aerosol scattering will be transmitted by the fast shutter. However, according to our calculations, the Rayleigh scattering alone should provide enough LGS photons without counting on extra return from aerosols.

We measured the UV transmission of the Glan-laser polarizers to be used with the Pockels cell. Polarizers from Red Optronics (a-BBO crystal) and Special Optics (calcite) transmit, respectively, 80-86% and 83-86% of light at 355 nm. To save valuable laser photons, we ordered polarizers with guaranteed transmission of 95% from Foctek Photonics.

3.2 Laser box and beam transfer

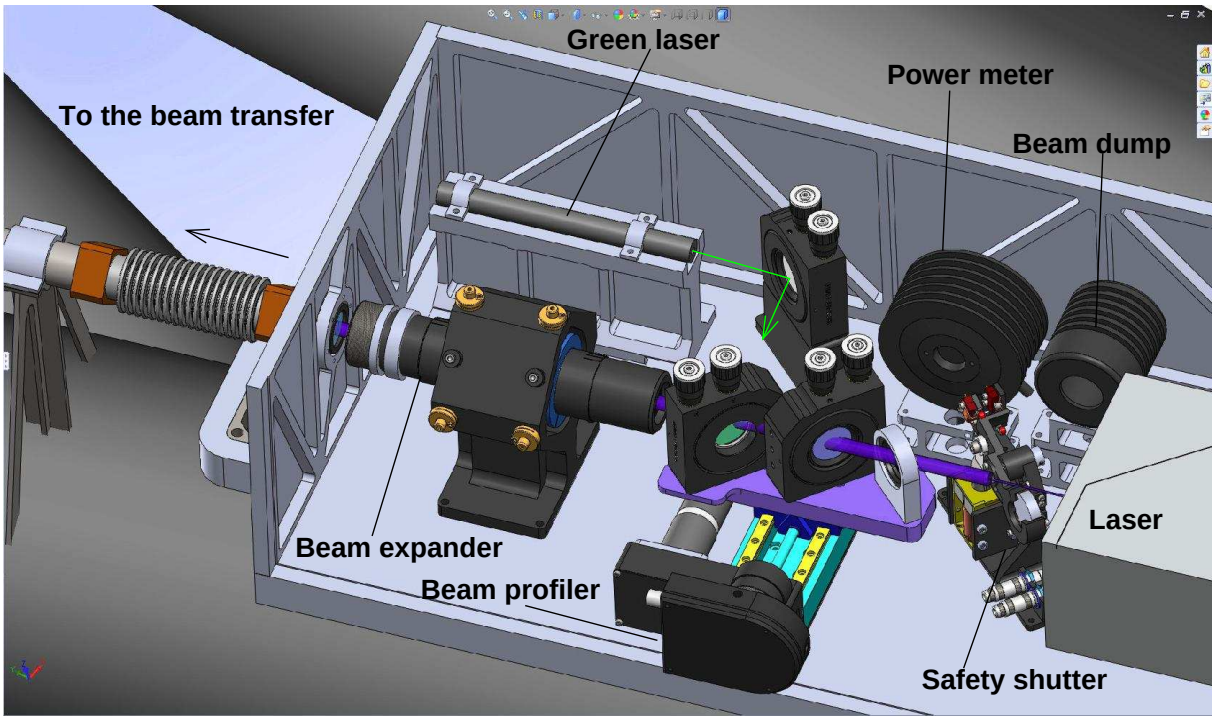

Figure 8. Design of the "laser box".

The laser will be located in a temperature-stabilized (heated) box attached to the telescope truss. Figure 8 shows the design of this box. The narrow laser beam is intercepted by the safety shutter consisting of a dielectric mirror and a beam dump. The shutter can be rapidly actuated by a solenoid. Once the shutter is opened, the beam enters the adjustable beam expander from Special Optics. The beam diameter is increased by 8 times and the collimated beam is sent to the laser launch telescope (LLT) with one additional reflection. The beam path is enclosed in metal tubes for protecting the optics and reducing stray light in the dome.

Three additional elements are mounted on a linear stage and can be inserted into the UV beam for testing, as shown in Fig. 8. In this configuration, the laser beam is deflected towards a power-meter (or dump) by a 99% sampler mirror; its transmitted part goes to the beam profiler for quality control. Meanwhile, a beam from the low-power 532 nm green laser replaces the UV beam. The green and UV beams will be adjusted to coincidence by means of two mirrors, so that the green laser can be used for alignment of the beam transfer train.

3.3 Laser launch telescope

The laser launch telescope (LLT) will be located in the limited space behind the secondary mirror of the SOAR telescope. The collimated laser beam expanded by 8 times reaches the LLT after only one reflection (see Fig. 10

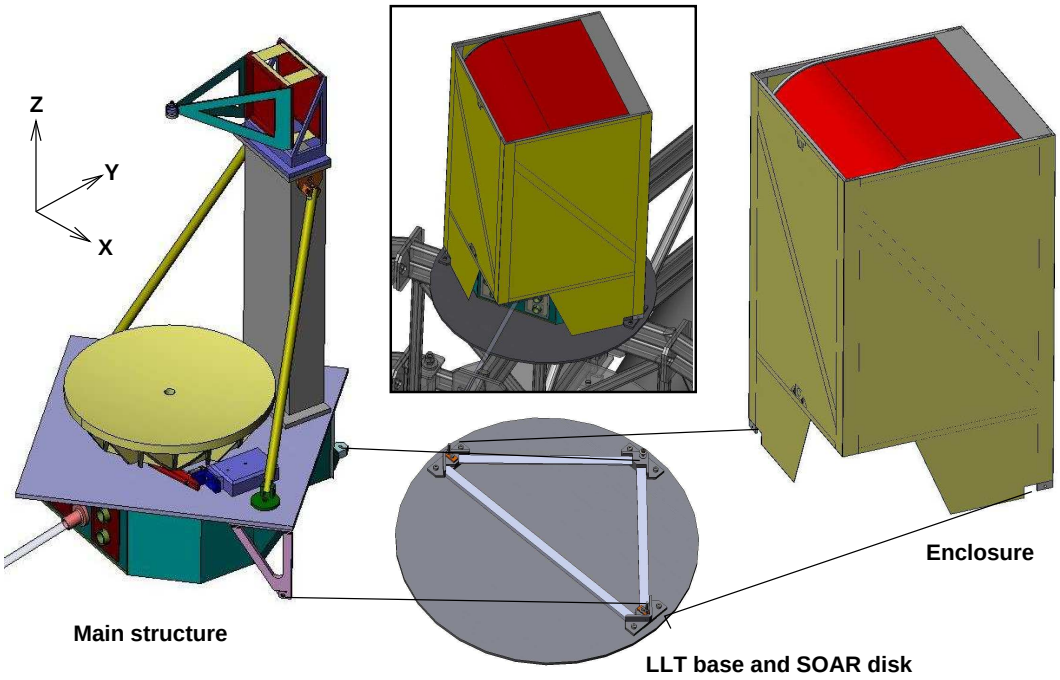

Figure 9. Mechanical design of the LLT.

in Ref. 10). We revised the initial LLT design, reducing the primary mirror diameter to 250 mm and shortening its focal length to 420 mm. The light-weighted primary mirror M1 is mounted on 3 actuated flexures, ensuring low deformations of theoptics due to gravity (Figs. 9,10). Lateral translations of the support points cause the mirror to "rotate" around its focus. This changes the LLT pointing without introducing off-axis coma. A 15-mm diameter spherical secondary mirror M2 is suspended by a prismatic vane structure which is attached by flexures and can move vertically for focusing. The focus actuator is located below the primary and is connected to the M2 vanes with an invar rod to reduce thermal focus drift.

Figure 10 illustrates some aspects of the LLT design. The parallel laser beam is reflected upwards from a dielectrically coated flat mirror M3. It is mounted on the piezoelectric tip-tilt platform S-330 from Physik Instrumente to allow fast steering of the LGS within a few arcseconds on the sky. Such steering is needed to maintain the LGS spots centered in the WFS in the presence of inevitable mis-alignments and flexure between LGS system and SAM. The slow component of the pointing error will be off-loaded to the the M1 actuators.

The M3 mirror transmits visible light. A parallel beam passing through M3 is intercepted by another flat mirror M3a and directed to a small "telescope" consisting of an achromatic lens and a CCD camera. This system will be used to check pointing, focus, and optical quality of the LLT by imaging bright stars when needed.

The LLT will be enclosed in a box-like shell. The opening will be sealed by a flexible shutter (red color in Fig. 9). The enclosure can be easily removed for service or cleaning. The LLT assembly is attached to the SOAR at three points, with compensation for differential thermal expansion between the steel telescope structure and the aluminum LLT frame. The LLT can be removed and installed in a reproducible way.

3.4 LGS wave-front sensor

The current SAM wave-front sensor, adapted for NGS, will be replaced by its LGS version, which is a bit more complex (Fig. 11). The return laser light is focused by the same triplet lens, but at a different distance and with a slightly different F-ratio. A weak lens is placed before focus to adjust the size of the pupil image on the lenslet array (LLA) for various LGS distances (from 7 km to 14 km). There is also a $\lambda/4$ plate for converting circularly-polarized light into linear polarization.

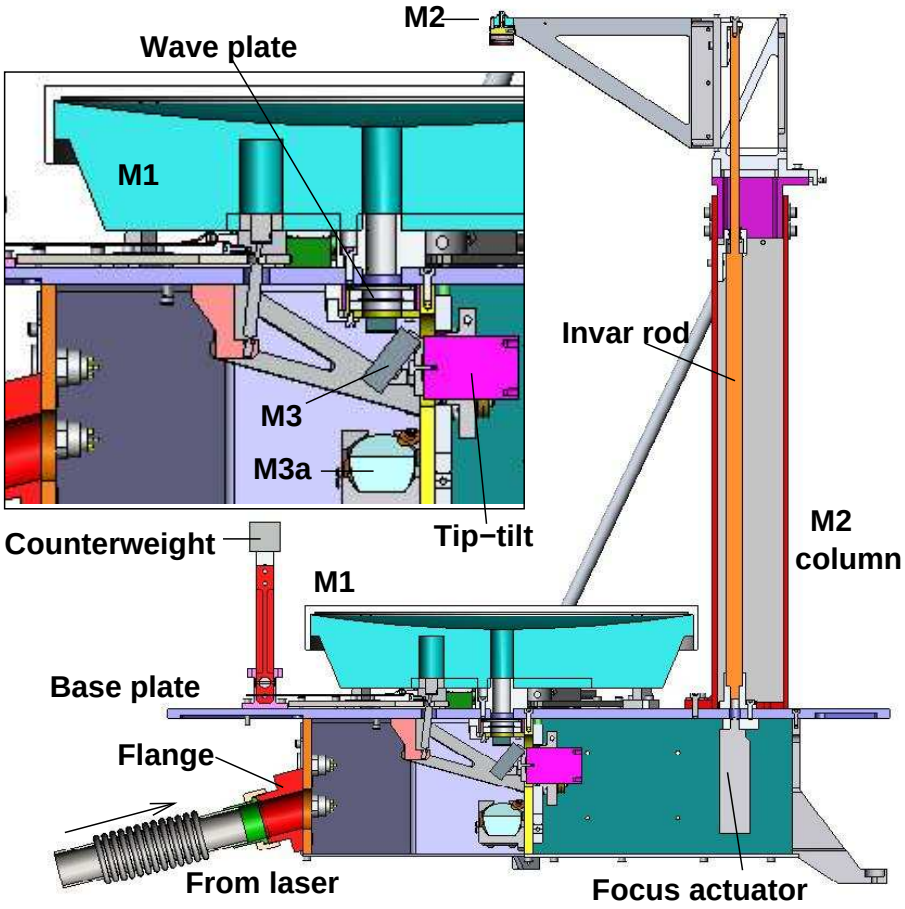

Figure 10. Cross-section of the LLT passing through the optical axis. The insert shows details.

The field of view is restricted by a small square aperture at the focus. During acquisition, a diagonal mirror slides in front of the aperture plate and directs the beam into the acquisition camera. At the same time, a reference point source is placed behind the aperture for WFS calibration.

The beam after focus is collimated by a singlet lens, goes through the fast shutter (Pockels cell between crossed polarizers) and is transformed again to match the LLA (the current assembly of CCD and LLA is used without modification).

4. CONCLUSIONS AND OUTLOOK

The SAM instrument is undergoing extensive tests in the laboratory. The components that were missing during the first-light experiment have now been integrated and tested. These are the two guide probes with quad-cell tip-tilt sensors and fiducial lights for probe location, and the atmospheric dispersion corrector (a pair of prisms in the collimated beam after dichroic). The CCD imager (4Kx4K e2v CCD with filter wheel and shutter) is in the final stages of fabrication. In parallel, we are integrating and testing the LGS WFS and LGS turbulence simulator – the components of the main module that will work with the LGS. We will install these sub-systems in SAM for tests and then return SAM to the NGS configuration. At this point, the instrument will be ready to go again at the telescope. We will proceed with commissioning SAM in the NGS mode and then re-configure it for the LGS operation without moving it back to the laboratory. SAM commissioning in the NGS mode will start in the 2nd half of 2010.

The optics of the LLT are being polished in the laboratory of S. Potanin in Moscow while its mechanics are being manufactured in La Serena. The whole LGS sub-system will be installed at the SOAR telescope and tested

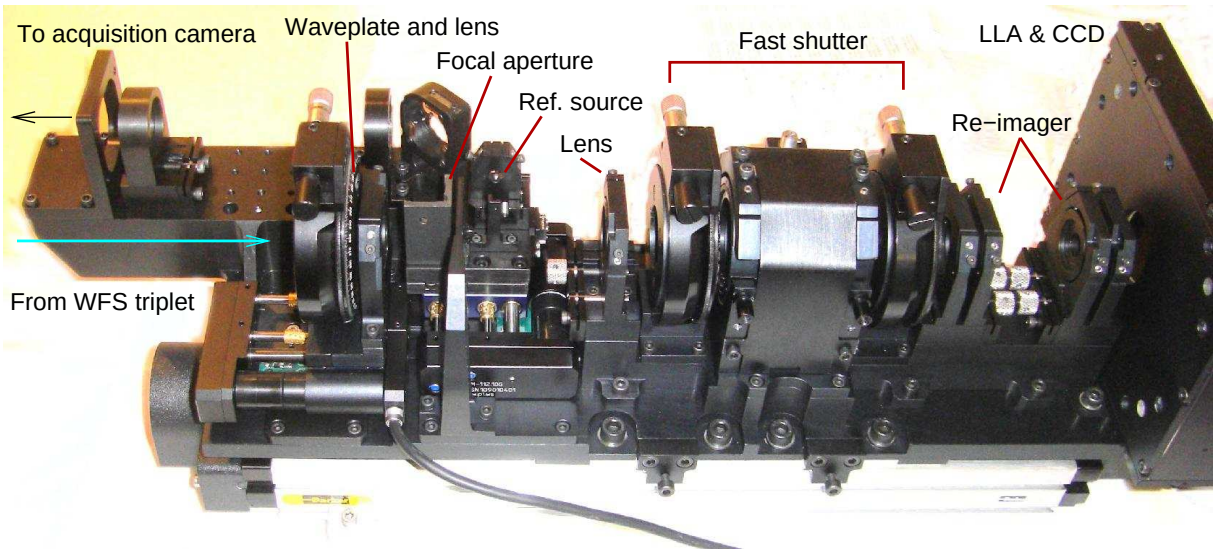

Figure 11. SAM LGS WFS ready for optical integration.

independently of the SAM AO module. Then the most interesting and challenging part of the SAM LGS testing will begin.

REFERENCES

[1] Baldwin, J.E., Warner, P.J., Mackay, C.D., "The point spread function in Lucky Imaging and variations in seeing on short timescales," Astron. Astrophys. 480, 589-597 (2008).

[2] Fusco, T., Rousset, G., Rabaud, D. et al., "NAOS on-line characterization of turbulence and adaptive optics performance," J. of Optics A: Pure Appl. Opt. 6, 585-596 (2004).

[3] Madec, P.-Y., "Control techniques,", in: [Adaptive Optics in Astronomy], ed. F. Roddier, Cambridge Univ. Press (1998).

[4] Noll, R.J., "Zernike polynomials and atmospheroic turbulence," JOSA 66, 207-211 (1976).

[5] Roddier, F., Northcott, M.J., Graves, J.E., McKenna, D.L., "One-dimensional spectra of turbulence-induced Zernike aberrations: time-delay and isoplanaticity error in artial adaptive compensation," JOSA(A) 10, 957-965 (1993).

[6] Tokovinin, A. Gregory, B. Schwarz, H., "Visible-light AO system for the 4.2-m SOAR telescope," Proc. SPIE 4839, 673-680 (2003).

[7] Tokovinin, A., Thomas, S., Gregory, B., van der Bliek, N., Schurter, P., Cantarutti, R., Mondaca, E., "Design of ground-layer turbulence compensation with a Rayleigh beacon," Proc. SPIE 5490, 870-878 (2004)

[8] Tokovinin, A., Travouillon, T., "Model of optical turbulence profile at Cerro Pachón," MNRAS 365, 1235-1242 (2006).

[9] Tokovinin, A., "Performance and error budget of a GLAO system," Proc. SPIE 7015, paper 77 (2008).

[10] Tokovinin, A., Tighe, R., Schurter, P., Cantarutti, R., van der Bliek, N., Martinez, M. Mondaca, E., Montane, A., "SAM - a facility GLAO instrument," Proc. SPIE 7015, paper 157 (2008).

[11] Tokovinin, A., Kellerer, A., Coudé Du Foresto, V., "FADE, an instrument to measure the atmospheric coherence time," Astron. Astrophys. 477, 671-60 (2008).

[12] Tokovinin, A., Cantarutti, R., "First speckle-interferometry at SOAR telescope with electron multiplictaion CCD," PASP 120, 170-177 (2008).

[13] Travouillon, T., Els, S., Riddle, R.L., Schöck, M., Skidmore, W., "Thirty Meter Telescope Site Testing VII: Turbulence Coherence Time," PASP 121, 787-796 (2009).